

## Reaction Coordinates and the Transition-Vector Approximation to the IRC

Willem-Jan van Zeist, Anton H. Koers, Lando P. Wolters, and  
F. Matthias Bickelhaupt\*

*Department of Theoretical Chemistry and Amsterdam Center for Multiscale Modeling,  
Scheikundig Laboratorium der Vrije Universiteit, De Boelelaan 1083,  
NL-1081 HV Amsterdam, The Netherlands,*

Received August 24, 2007

**Abstract:** The appearance of a reaction profile or potential energy surface (PES) associated with the reaction path (defined as the path of steepest descent from the saddle point) depends on the choice of reaction coordinate onto which the intrinsic reaction coordinate is projected. This provides one with the freedom, but also the problem, of choosing the optimal perspective (i.e., the optimal reaction coordinate) for revealing what is essential for understanding the reaction. Here, we address this issue by analyzing a number of different reaction coordinates for the same set of model reactions, namely, prototypical oxidative addition reactions of C–X bonds to palladium. We show how different choices affect the appearance of the PES, and we discuss which qualities make a particular reaction coordinate most suitable for comparing and analyzing the reactions. Furthermore, we show how the transition vector (i.e., the normal mode associated with a negative force constant that leads from the saddle point to the steepest descent paths) can serve as a useful and computationally much more efficient approximation (designated TV-IRC) for full IRC computations, in the decisive region around the transition state.

### 1. Introduction

The terms “reaction profile” or “potential energy surface” are habitually used when chemical reactions are discussed. The first step toward understanding a reaction mechanism is locating the stationary points on the system’s potential energy surface (PES).<sup>1</sup> On the entire PES, three stationary points are required to characterize the core reactivity parameters of a typical reaction, namely, the reactants, transition state (TS), and products. These stationary points provide one with the reaction energy and the activation barrier.

For a deeper understanding of the reaction, it is desirable to find connecting pathways between these points on the PES. This enables one to examine how exactly the reactants transform into the TS and then into the products. A reaction path is also an important ingredient, for example, in the extended activation strain model in which trends in activation

barriers are described and understood in terms of how the original reactants affect each other along such a path.<sup>2,3</sup>

The most common approach is finding the intrinsic reaction path (IRP) between a saddle point (transition state) and the minimum in an adjacent valley (reactants or products) on the PES. This path is defined as the path of steepest descent from the TS to the minima and is found, in mass-weighted Cartesian coordinates, through intrinsic reaction coordinate (IRC) calculations.<sup>4–7</sup> The IRP has been successfully used in many studies as the reaction path.<sup>8</sup> The reaction profile or PES of the reaction can now be obtained, for example, by plotting the system’s energy as a function of the IRC. Now that IRC calculations for larger systems become feasible, analysis of the IRP becomes an ever increasingly important topic.<sup>9</sup>

Once the reaction path (i.e., path of steepest descent) has been computed, we can in principle plot the energy along this path. This yields the reaction profile or PES of the reaction. However, the appearance of a reaction profile or PES associated with the reaction path depends on the choice

\* Corresponding author. fax: +31-20-5987629, e-mail: FM.Bickelhaupt@few.vu.nl.

of reaction coordinate onto which the IRC, which defines the reaction path, is projected. This provides one with the freedom, but also the problem, of choosing the optimal perspective, that is, the optimal reaction coordinate, for revealing what is essential for understanding the reaction. The reaction coordinate is a means for a chemist to refer to the extent of progress of a reaction using one parameter. This may be chosen on intuitive grounds, and often it is not even explicitly quantified but used in a qualitative fashion. In computational studies, still, the IRC itself features as the reaction coordinate for plotting the energy or other properties of a system along the IRP. Indeed, the IRC is a well-defined and quantitative choice of a reaction coordinate since it precisely defines all geometrical changes along the IRP. However, the IRC does not discriminate between those deformations that constitute the core geometrical transformation associated with the reaction and other changes in geometry that may be large but not critical. Furthermore, the IRC is multidimensional in terms of simple geometry parameters and therefore less transparent.

In the present paper, prompted by earlier investigations on reactivity,<sup>2,3,10,11</sup> we address the issue of how to choose the reaction coordinate such that it is optimal for monitoring and recognizing those events and phenomena that determine a reaction, in particular the barrier height. Note, once more, the difference between the reaction *path* (i.e., the uniquely defined IRP from an IRC calculation) and the reaction *coordinate*, which serves to optimally represent properties along the reaction path, such as the energy (i.e., the reaction *profile*). Here, we elaborate on the issue of how this reaction coordinate is to be chosen. In practice, understanding differences between reactions (e.g., trends in barriers) is even more important, and a clever choice of reaction coordinate is key to understanding the observed differences between these reactions. Here, we anticipate that indeed certain choices of reaction coordinates reveal features that are associated with critical moments along the IRP, while others hide them.

Thus, we have investigated and compared the IRPs of four series of organic and organometallic reactions: (i) the oxidative addition of the C–C bonds of ethane, propane, methylpropane, and dimethylpropane to palladium via direct oxidative insertion (OxIn); (ii) the oxidative addition of the methane C–H, chloromethane C–Cl, fluoromethane C–F, and silane Si–H bonds to palladium via the OxIn mechanism; (iii) the oxidative addition of the methane C–H, chloromethane C–Cl, and silane Si–H bonds via an alternative S<sub>N</sub>2-type pathway; (iv) nucleophilic substitution of Cl<sup>−</sup> with chloromethane and with chloroethane. This is done through IRC calculations with the Amsterdam Density Functional (ADF) program, using density functional theory at BLYP/TZ2P.<sup>12,13</sup>

Furthermore, we have explored the validity of the so-called transition-vector approximation to the intrinsic reaction coordinate (TV-IRC). The TV-IRC approximation consists of using the transition vector (i.e., the one and only normal mode with a negative eigenvalue that characterizes the transition state) instead of the full IRC in the region “before and after” the transition state. The TV-IRC approximation

leads to an enormous reduction in computational cost of analyses along the IRP, in particular for larger, more realistic model reactions. But, of course, its validity depends on how well and, in particular, over which range the transition vector is really a good approximation to the IRC. We discuss both successful applications as well as situations that lead to a breakdown of the TV-IRC approximation.

## 2. Computational Details

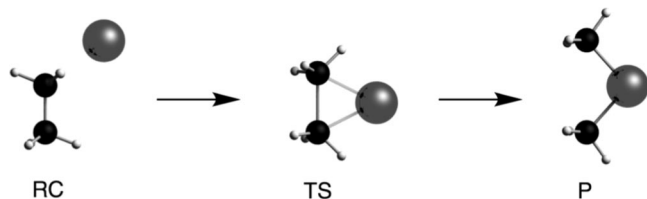
The IRPs were generated through IRC calculations, with the ADF program.<sup>12,13</sup> The BLYP<sup>14</sup> functional was used in combination with a TZ2P basis set. The latter is of triple- $\zeta$  quality and has been augmented with two sets of polarization functions: 2p and 3d on hydrogen; 3d and 4f on carbon, chlorine, oxygen, fluorine, and phosphorus; and 5p and 4f on palladium.<sup>15</sup> The core shells of carbon (1s), fluorine (1s), chlorine (up to 2p), silicon (up to 2p), and palladium (up to 3d) were treated by the frozen-core approximation.<sup>15</sup> Scalar relativistic effects were taken into account by the zeroth-order regular approximation.<sup>16</sup> This approach has been shown to give accurate results for the systems under consideration.<sup>17</sup> The reaction profiles, and analysis thereof, were generated using the PyFrag program.<sup>18</sup>

The IRC is constituted by the trajectory in mass-weighted coordinates, orthogonal to the equipotential contours of a PES, that connects two energy minima through a common TS from which it slopes downward along the steepest descent lines in  $3N - 6$  configurational space ( $N$  = number of atoms).<sup>5</sup> The IRC method in ADF is based on the work by Fukui<sup>5</sup> and has been implemented in the ADF package by Deng and Ziegler<sup>4</sup> using mass-weighted coordinates and the constrained search method of Gonzalez and Schlegel.<sup>6</sup> In Cartesian coordinates, the mass-weighted coordinates are defined for each atom A as  $X_A = m_A^{1/2}x_A$ ,  $Y_A = m_A^{1/2}y_A$ , and  $Z_A = m_A^{1/2}z_A$  with  $x_A$ ,  $y_A$ , and  $z_A$  the nonmass-weighted Cartesian coordinates.

The electron density distribution is analyzed using the Voronoi deformation density (VDD) method.<sup>19</sup> The VDD charge  $Q_A$  is computed as the (numerical) integral of the deformation density  $\Delta\rho(\mathbf{r}) = \rho(\mathbf{r}) - \sum_B \rho_B(\mathbf{r})$  associated with the formation of the molecule from its atoms in the volume of the Voronoi cell of atom A (eq 1). The Voronoi cell of atom A is defined as the compartment of space bounded by the bond midplanes on and perpendicular to all bond axes between nucleus A and its neighboring nuclei.

$$Q_A = \int_{\text{Voronoi-cell-A}} [\rho(r) - \sum_B \rho_B(r)] dr \quad (1)$$

Here,  $\rho(\mathbf{r})$  is the electron density of the molecule and  $\sum_B \rho_B(\mathbf{r})$  the superposition of atomic densities  $\rho_B$  of a fictitious promolecule without chemical interactions that is associated with the situation in which all atoms are neutral. The interpretation of the VDD charge  $Q_A$  is rather straightforward and transparent. Instead of measuring the amount of charge associated with a particular atom A,  $Q_A$  directly monitors how much charge flows, due to chemical interactions, out of ( $Q_A > 0$ ) or into ( $Q_A < 0$ ) the Voronoi cell of atom A, that is, the region of space that is closer to nucleus A than to any other nucleus.

**Scheme 1.** Stationary Points in the Oxidative Insertion of Pd + Ethane

### 3. Choosing a Suitable Reaction Coordinate

To illustrate our thoughts, we will use four very similar varieties of an oxidative insertion reaction. Starting off with the oxidative insertion of palladium into the C–C bond of ethane, we consider the reactions where the hydrogens on one side of ethane are subsequently substituted by methyl groups. We thereby get a series of oxidative insertions of palladium into the C–C bonds of ethane, propane, methylpropane, and dimethylpropane. These reactions proceed from a reaction complex (RC) at ca.  $-6$  kcal/mol relative to reactants, via a TS at around 20 up to some 30 kcal/mol depending on the alkane, toward the product (P) at ca.  $-10$  kcal/mol (see Scheme 1). In terms of geometrical changes, this reaction is in the first place defined by the breaking of the C–C bond into which the metal inserts, as can be seen in Scheme 1.

In the following, we examine three perspectives on the reaction profiles that differ in the choice of the reaction coordinate onto which the IRC has been projected (see Figure 1): (a) the IRC itself and (b, c) two different projections of the IRC on simple geometry parameters. In all cases, the reaction profiles run from the reactant complex at the left to the product at the right.

In Figure 1a the reaction profiles are plotted as functions of the IRC itself as the reaction coordinate. Note that we display the progress of the reaction relative to the RC and not, as is often done, relative to the transition state, which technically is the starting point of an IRC calculation. The reason is that, for our purposes, namely, understanding the progress of a reaction and the height of the barrier in terms of the reactants, it is essential to take these reactants or the precursor complex as the point of reference. For completeness, we show all IRC graphs with the TS in the center in the Supporting Information. The IRC is the accumulative distance between the IRC points in mass-weighted Cartesian coordinates (see section 2). Note that the reaction profiles based on the IRC as the reaction coordinate vary rather chaotically from one reaction to the other. This behavior can be explained by the geometry changes along the reaction path. For example, in the case of propane, the TS peak is shifted toward the product side, that is, to a higher value of the reaction coordinate. The origin of this apparent “irregularity” is that one methyl group rotates freely over large parts of the reaction, thus creating a large coordinate distance in the IRC while influencing the total energy only very little. This can be seen in Scheme 2, which shows snapshots along the IRC of the reaction system starting from the RC until just before the TS is reached. This also illustrates the main problem: the IRC traces *all* movement of all of the nuclei in

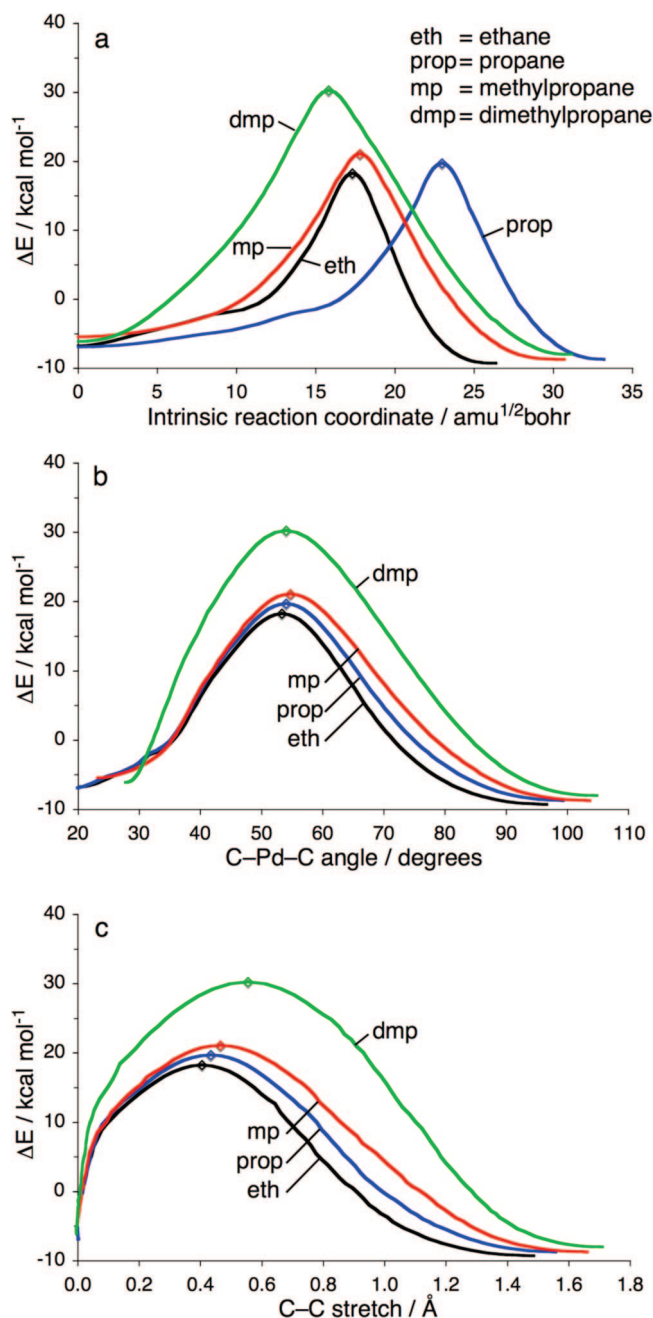


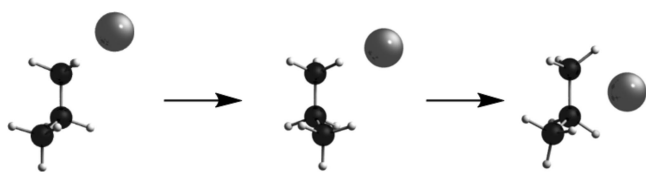
**Figure 1.** Comparison of three reaction coordinates for representing the PES of the oxidative insertion (OxIn) of Pd into the central C–C bond of ethane (black, eth), propane (blue, prop), methylpropane (red, mp), and dimethylpropane (green, dmp): (a) IRC distance (mass-weighted au) starting from the reactant complex, (b) bond angle C–Pd–C (in deg), (c) C–C bond stretch relative to substrate (in Å).

the reaction whether this is intrinsic to the actual process of bond breaking and insertion or just a derivative of the latter. Although there is some information to be gathered from these graphs, they are not really suitable to catch (the trends in) the essence of the various reactions. A more detailed discussion of this issue can be found in ref 20.

Next, in our quest for reaction coordinates that uncover the systematic trends in the oxidative insertion process, we examine projections of the IRC onto simple geometry parameters. We recall that the reaction coordinate should have significant amplitude in (and correlate with) the IRC-



**Scheme 2.** Snapshots along the IRC of the Oxidative Insertion of Pd + Propane, from the RC till just before the TS



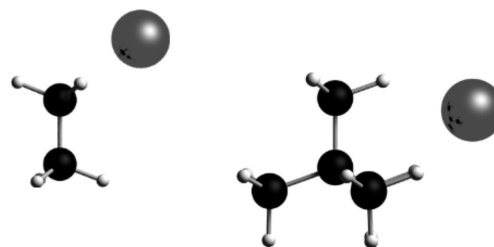
defined reaction path, such that it is a reliable measure of the progress of the reaction. Also, the reaction coordinate should provide us with insight into when and how the underlying features in the electronic structure (e.g., metal–substrate donation and backdonation orbital interactions) are active and decisive in determining the shape of the PES, in particular, the geometry of the TS and its energy. To this end, it is best to examine reaction profiles obtained with various choices of reaction coordinates which, in ADF 2007.01,<sup>12</sup> can be straightforwardly done with the ADFmovie tool. It can also be instructive to plot various geometrical parameters against each other. This can give nice insight into how the various geometrical features play a role, compared to each other, along the reaction path.

Two geometry parameters emerge as good candidates for a reaction coordinate: (i) the C–Pd–C angle, which increases as palladium approaches and the C–C bond expands, and (ii) (the stretch in) the C–C distance. This is of course not entirely unexpected in view of the fact that (i) the C–C bond breaking is an essential geometrical deformation which defines the oxidative insertion reaction and (ii) the C–Pd–C angle strongly correlates with the C–C distance on a large part of the reaction path.

Figure 1b shows the reaction profile as a function of the C–Pd–C angle as the reaction coordinate. It is immediately clear that the resulting reaction profiles (Figure 1b) behave much more systematically than in the previous representation (Figure 1a). From ethane to propane to methylpropane, there is a systematic and gradual change in the reaction profiles: they all start more or less at the same point but become higher in energy along this series. Furthermore, the TS shifts stepwise to the right, that is, to the product side. But the reaction profile for dimethylpropane is different, in particular at lower bond angles or, in other words, near the reactant complex. This is because palladium coordinates in a  $\eta^3$  manner to the C–H bonds of three different methyl groups of dimethylpropane, as compared to the  $\eta^2$  coordination with ethane (see Scheme 3), such that it is from the beginning closer to the C–C bond into which it inserts. Therefore, it has to reorient (and “travel”) less in order to reach the TS, as can be seen in IRC movies (not shown) and also in the reaction profile based directly on the IRC as the reaction coordinate (see Figure 1a). The C–Pd–C bond angle is a reaction coordinate that magnifies differences in the reactant-complex region, that is, in early stages of the reaction. The height of the barrier is however determined beyond the RC, at a more advanced stage of the reaction.<sup>2,3</sup>

Figure 1c shows the reaction profile as a function of the C–C bond stretch (relative to the reactants) as the reaction coordinate. The reaction profiles vary very systematically

**Scheme 3.**  $\eta^2$  and  $\eta^3$  Coordination in Reactant Complexes of Pd + Ethane (left) and Pd + Dimethylpropane (right)



from one reaction to another. Now, they all start at the same point (in the reactants, the C–C bond is not yet stretched), and there is both a systematic increase in barrier height and a systematic shift to the right of the transition states. The systematic increase in energy and position along the C–C reaction coordinate is intimately connected with how the strain energy of the substrate varies and how the bonding capabilities of the substrate with the metal evolve. This has been previously pointed out in an activation strain analysis of C–H and C–C bond activation.<sup>3</sup> This explains the very systematic and smooth change in reaction profiles along the four reactions. A more detailed examination of the geometrical changes along the C–C reaction coordinate shows that this reaction coordinate magnifies the region along the IRC reaction path where the TS is located, that is, where the height of the barrier is determined, whereas the very early stage near the RC is more compressed. This is due to the fact that, during the first part of the reaction, the C–C bond does not change much, while the geometry of the reactant complex can change significantly due to migration of the metal from the optimal coordination site toward the point where it starts to insert into the C–C bond.

Next, we compare the oxidative insertion reactions of palladium into the C–H, C–C, C–F, and C–Cl bonds in methane, ethane, fluoromethane, and chloromethane, respectively.<sup>3</sup> The resulting PESs are again displayed as a function of the IRC as well as projections thereof onto the C–Pd–X angle and onto the C–X bond stretch relative to the reactant complex (see Figure 2). In addition, to the energy of the reaction system (i.e., the PES), we plot here also the VDD atomic charge of palladium and the population of the substrate's C–X antibonding  $\sigma^*_{C-X}$  acceptor orbital that becomes occupied in the course of the reaction.

The two main features in the metal–substrate bonding mechanism are, as has been briefly mentioned above, (i) the *backdonation* of charge from the palladium 4d orbital into the  $\sigma^*_{C-X}$  antibonding orbital of the C–X bond that is being broken and (ii) the donation of the  $\sigma_{C-X}$  orbital into the 5s orbital of palladium. Charge transfer and orbital populations are consequently quantities that are associated with the extent of progress of the oxidative-insertion reaction on the level of the electronic structure. The increasing population of the antibonding orbital shows in essence the bond-breaking process. All of these quantities are in the first place dependent on the (stretch in) C–X distance in the substrate. This is nicely illustrated in Figure 2, which shows plots of palladium VDD atomic charges<sup>19</sup> and  $\sigma^*_{C-X}$  antibonding orbital populations for each of the reaction coordinates. It is easily

seen that the C–X bond stretch allows us to represent the bond breaking process in the most smooth and consistent manner (see Figure 2g–i). Choosing the IRC on the  $x$  axis again leads to more chaotic variation along the different C–X bonds because the progress of the reaction, that is, the way in which the energy, atomic charge, and orbital population change, is directly linked to the C–X stretch and not to all of the other geometry parameters that contribute to the IRC (see Figure 2a–c). The C–Pd–X bond angle yields again a more smooth description (see Figure 2d–f), but the systematics of the bonding mechanisms underlying the reaction in progress come out best in the plots that are based on the C–X stretch.

Furthermore, the C–X bond stretch is the main (but not the only!) determinant for the strain energy  $\Delta E_{\text{Strain}}(\zeta)$  of the, along the reaction path, increasingly deformed substrate, which together with the metal–substrate interaction  $\Delta E_{\text{int}}(\zeta)$  determines the reaction profile or potential energy surface  $\Delta E(\zeta) = \Delta E_{\text{Strain}}(\zeta) + \Delta E_{\text{int}}(\zeta)$  along the reaction coordinate  $\zeta$  (cf. activation strain model, refs 2 and 3). Thus, the C–X stretch emerges as the optimal choice for representing the reaction profile and underlying features in the electronic structure for oxidative insertion reactions.

In the next example, we compare the oxidative addition of the methane C–H and chloromethane C–Cl bonds, each via two competing reaction mechanisms: direct OxIn and an alternative  $S_N2$  mechanism (see Figure 3).<sup>3,11</sup> The  $S_N2$

mechanism of Pd + CH<sub>4</sub> actually leads to the dehydrogenation of methane and yields molecular hydrogen plus a palladium–carbene complex (see Scheme 4). In the case of Pd + CH<sub>3</sub>Cl, the actual substitution process is followed directly (i.e., without the occurrence of an intermediate  $S_N2$  product complex) by a rearrangement of the expelled chloride leaving group toward the palladium atom to which it eventually coordinates (see also the snapshots in Figure 5d). The TS of the overall process occurs in the second stage, that is, during the migration of Cl<sup>−</sup> toward Pd. Here, we see that both the IRC and the C–Pd–X bond angle yield a relatively disorderly picture in which no clear trends become apparent (see Figure 3). The C–X bond stretch, on the other hand, results in a more systematic appearance of the reaction profiles as well as the atomic charge and orbital population analyses (see Figure 3). The latter two show again that this reaction coordinate captures the essence of the reactions, namely, activation and rupture of the C–X bond through its reduction (i.e., through population of the  $\sigma^*_{\text{C-X}}$  orbital of the substrate). Note that this holds in particular also for the  $S_N2$  pathway. An interesting phenomenon that occurs in the case of the  $S_N2$  processes at CH<sub>3</sub>Cl is the curling back of the curves near the end, that is, to the right in the representation as a function of the C–X stretch (see Figure 3g–i). This is a reflection of the fact that after the TS has been passed the  $S_N2$ -rearrangement pathway merges into the OxIn pathway. This is accompanied by a reduction of the

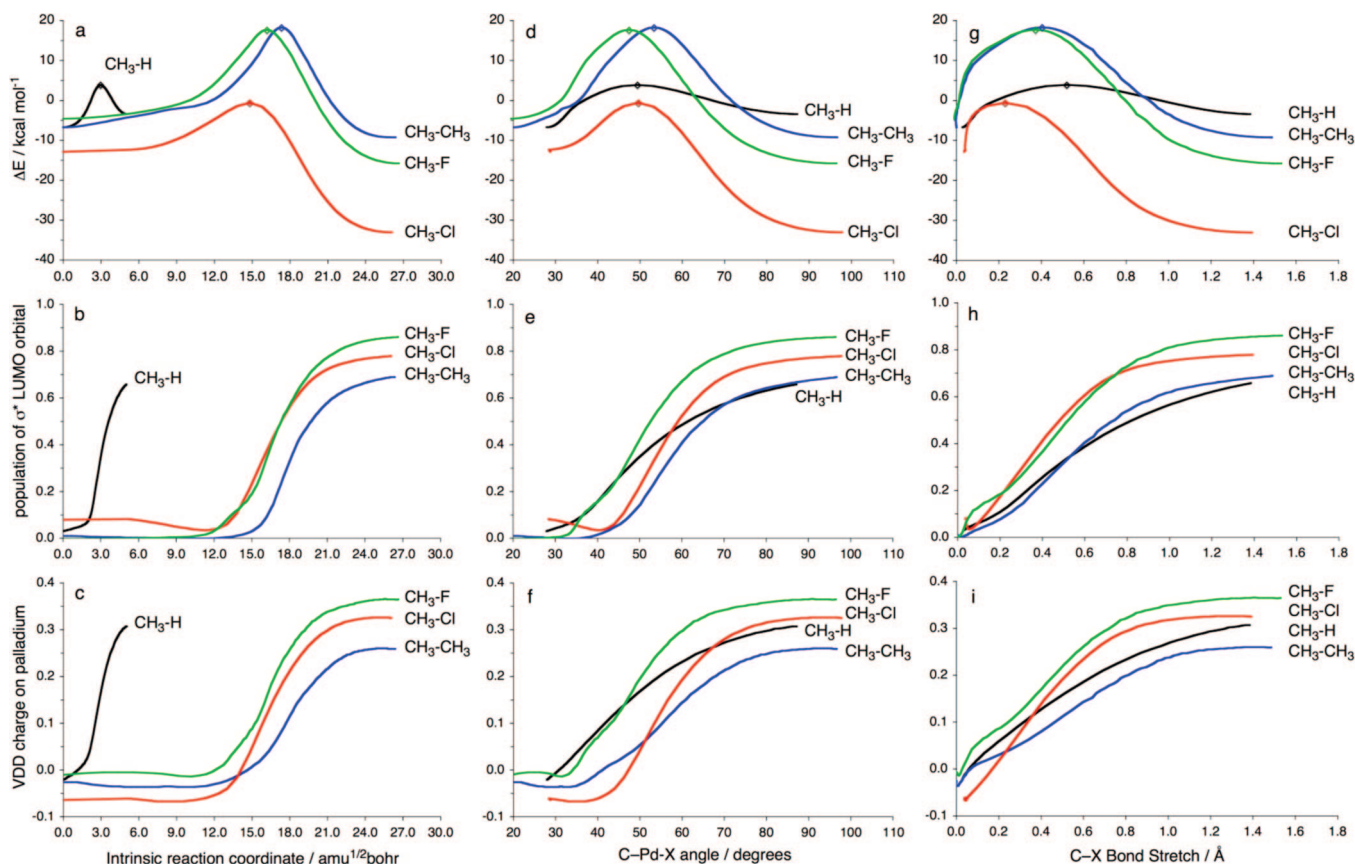


**Figure 2.** Comparison of three reaction coordinates for representing the PES and other properties of the oxidative insertion (OxIn) of Pd into the methane C–H (black), ethane C–C (blue), fluoromethane C–F (green), and chloromethane C–Cl bonds (red): (a, b, c) IRC distance (mass-weighted au) starting from the reactant complex, (d, e, f) bond angle C–Pd–X (in deg), and (g, h, i) C–X bond stretch relative to substrate (in Å). The plots show (a, d, g) the PES, (b, e, h) the population of the C–X  $\sigma^*$  antibonding LUMO, and (c, f, i) the VDD charge of the Pd atom.

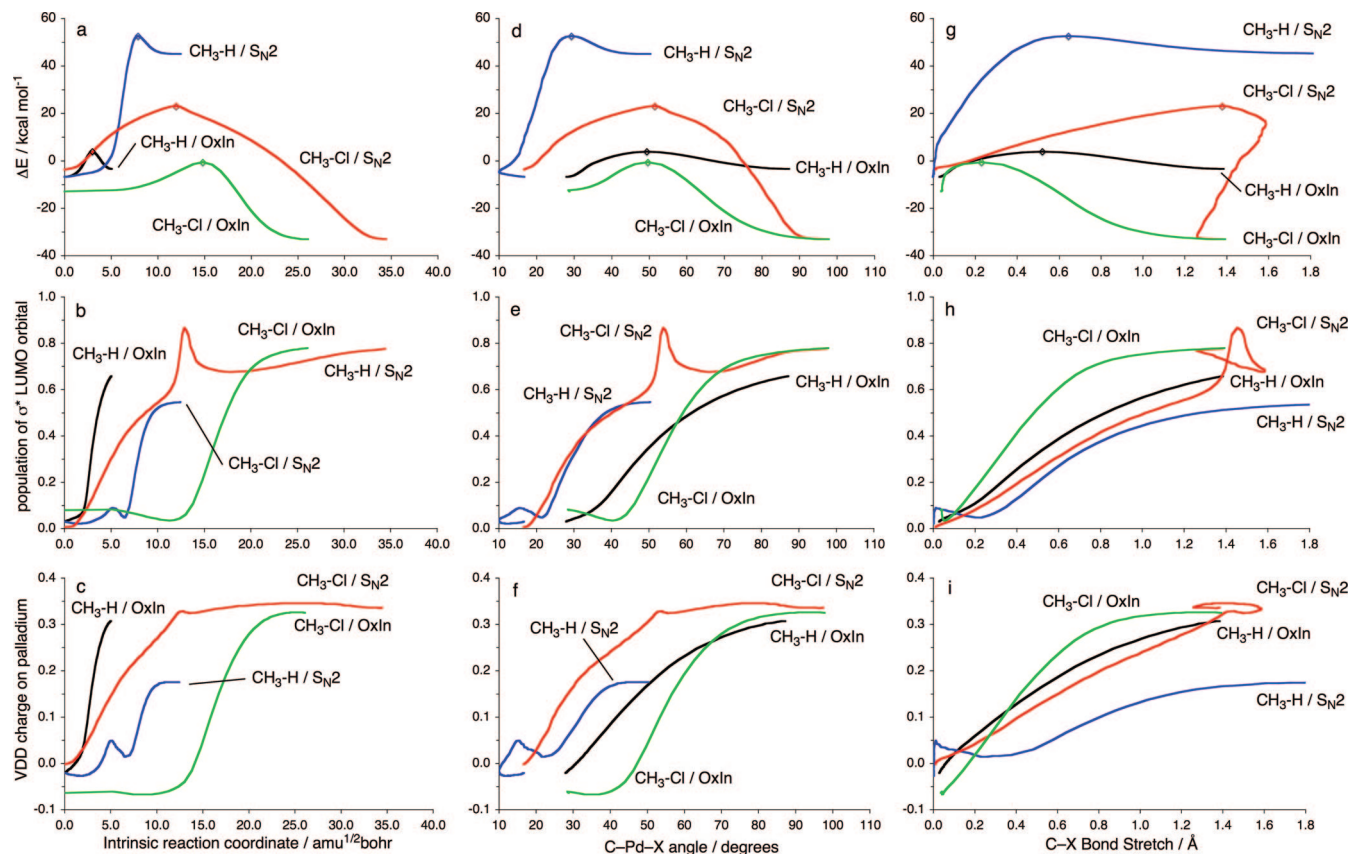
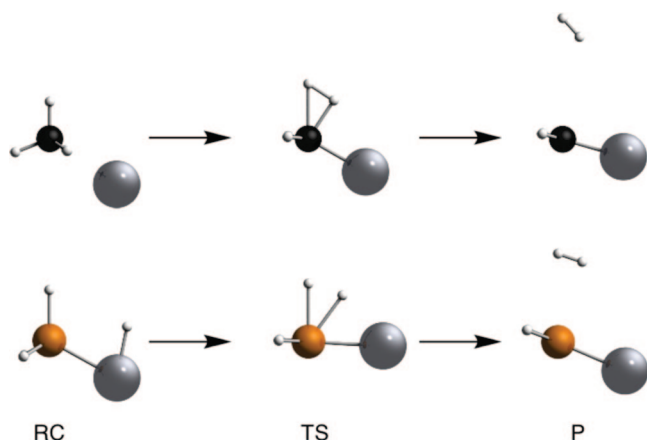


**Figure 3.** Comparison of three reaction coordinates for representing the PES and other properties of the oxidative insertion (OxIn) of Pd into methane C–H (black) and chloromethane C–Cl (green) as well as oxidative addition via  $S_N2$  substitution of Pd with methane C–H (blue) and chloromethane C–Cl bonds (red): (a, b, c) IRC distance (mass-weighted au) starting from the reactant complex, (d, e, f) bond angle C–Pd–X (in deg), and (g, h, i) C–X bond stretch relative to the substrate (in Å). The plots show (a, d, g) the PES, (b, e, h) the population of the C–X  $\sigma^*$  antibonding LUMO, and (c, f, i) the VDD charge of the Pd atom.

**Scheme 4.** Stationary Points in the Pd-Induced Dehydrogenation of  $CH_4$  (upper) and  $SiH_4$  (lower)



C–Cl distance during the migration of the  $Cl^-$  leaving group (i.e., the curling back). Note that, after the migration stage is finished, the curve of the  $S_N2$  pathway is superimposed on that of the OxIn pathway. The sudden increase of the  $\sigma^*_{C-X}$  orbital population takes places around the transition state point, where the C–Cl bond is also formally, that is, electronically, broken in the sense that we have a configuration switch toward a reduced C–Cl bond. For a detailed analysis of these curves, see ref 3.

Finally, we compare the activation of the methane C–H and silane Si–H bonds, again for each bond via the two competing OxIn and  $S_N2$  pathways.<sup>8</sup> As noted in the previous example, the  $S_N2$  reaction of Pd +  $CH_4$  leads to the dehydrogenation of methane (see Scheme 4). The oxidative insertion proceeds without a barrier for Pd +  $SiH_4$ . Therefore, in this case, the IRC computations were started from an artificial reactant complex in which Pd coordinates end-on to a Si–H bond yielding a  $C_{3v}$  symmetric species  $Pd \cdots H-SiH_3$ . This species is a second-order saddle point with two degenerate imaginary frequencies, both corresponding to a mode that leads to the OxIn product. Thus, the overall  $S_N2$  reaction proceeds from the reactants, via the product of OxIn that plays the role of a precursor complex, toward an  $S_N2$ -type TS that, just as in the case of methane, eventually leads to dehydrogenation (see Scheme 4). Figure 4 shows the reaction profiles corresponding to the four pathways plotted as a function of the IRC, A–Pd–H angle, and A–H stretch. Similar to previous series of reactions, trends come out in the most systematic manner if PESs are plotted as a function of the A–H stretch. Activation strain analyses have shown that the higher energies of the reaction profiles involving methane are, among others, due to the fact that dissociating the C–H bond is inherently connected with a higher strain because this bond is stronger than the Si–H bond.<sup>8</sup>



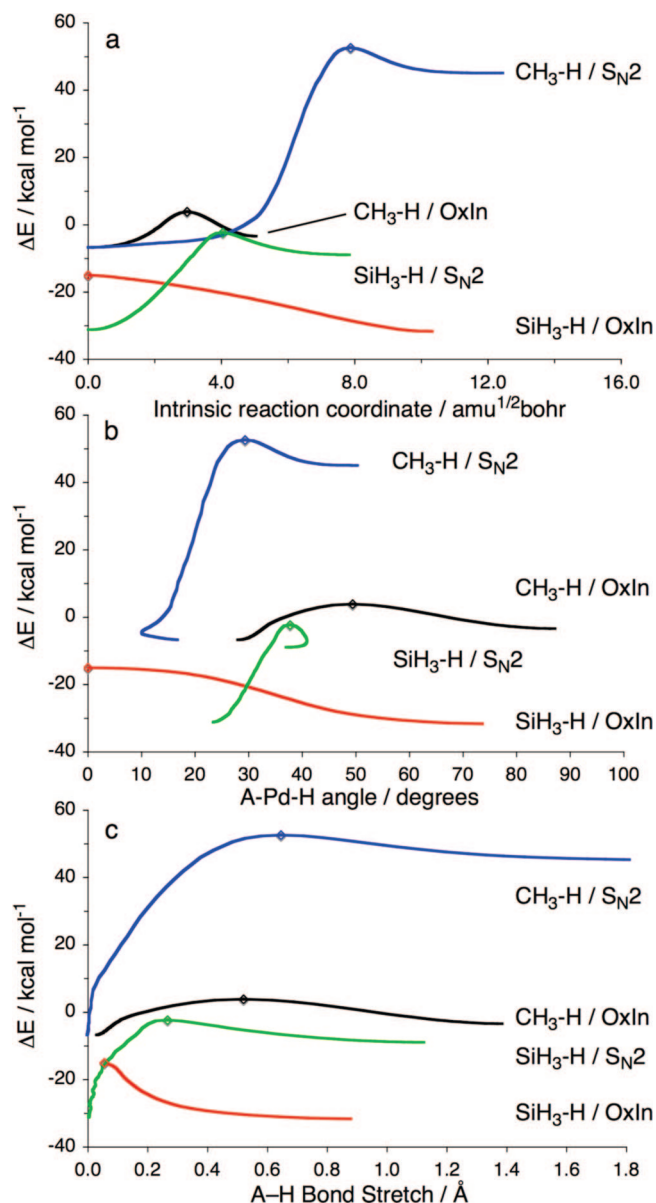


**Figure 4.** Comparison of three reaction coordinates for representing the PES of the oxidative insertion (OxIn) of Pd into the methane C–H (black) and silane Si–H (red) as well as the  $S_N2$ -type reactions of Pd with the methane C–H (blue) and silane Si–H bonds (green): (a) IRC distance (mass-weighted au) starting from the reactant complex, (b) bond angle C–Pd–X (in deg), and (c) C–X bond stretch relative to the substrate (in Å). See Scheme 4 for snapshots of stationary points.

#### 4. Transition Vector as Approximation to IRC

Vibrational analysis reveals that C–C stretching also has a large amplitude in the transition vector of our oxidative insertion reactions, that is, the normal mode associated with a negative force constant that leads from the saddle point to the steepest descent paths. Thus, for very large model reaction systems for which IRC calculations become prohibitively expensive (or just impossible), following the path defined by the TV may be used as an approximation of that IRC in the region “around the TS”. In fact, we find that the TV path approximates the IRC path very well over a

sufficiently long interval to be useful for representing and analyzing the reaction profile of our oxidative insertion reactions. Numerical experiments show that the reaction profile of oxidative insertion reactions (as a function of the C–C stretch and the C–Pd–C angle as the reaction coordinates) generated on the basis of the TV essentially coincides with that generated on the basis of the full IRC over an interval of about 0.5 Å of the C–C reaction coordinate around the TS (see Figure 5a and b). We designate this procedure as the TV-IRC approximation. Since TV-IRC calculations typically require around 10 single-point calculations only, the computational cost is dramatically decreased as compared to the corresponding partial IRC (let alone a full IRC), which would then require several constrained geometry optimizations in a stage of the reaction that goes with relatively strong structural reorganization on a shallow saddle region of the PES.

Interestingly, the TV-IRC reaction profile agrees over a longer interval with the IRC reaction profile if it is represented as a function of the C–C stretch (agreement over roughly one-third of the entire reaction interval!) than if it is represented as a function of the C–Pd–C angle (agreement over roughly one-fifth of the entire reaction interval, compare part a of Figure 5 with part b). This is consistent with the fact that the C–C stretch plays a more important role near the TS and that the reaction profile as a function of this reaction coordinate zooms in on the region around the TS.

We have also tested the TV-IRC approximation for other classes of reactions. In Figure 5c, we show the reaction profiles for the  $S_N2$  reactions of  $\text{Cl}^- + \text{CH}_3\text{Cl}$  and  $\text{Cl}^- + \text{CH}_3\text{CH}_2\text{Cl}$  as functions of the C–Cl (i.e., carbon-leaving group) stretch. Again, the TV-IRC-based reaction profiles coincide with the IRC-based ones over a range of some 0.5 Å of the reaction coordinate, that is, roughly one-third of the entire reaction interval.

Finally, we also wish to stress the situations in which the TV-IRC approximation breaks down. This happens whenever the character of the geometrical deformations changes quickly or drastically along the reaction path. Typically, this happens when different elementary steps merge into one reaction step. An example is the alternative  $S_N2$  mechanism for the oxidative addition of  $\text{Pd} + \text{CH}_3\text{Cl}$ . For the oxidative insertion mechanism, as can be seen in Figure 5d, the TV-IRC-based reaction profile again nicely coincides with the IRC-based one. At variance, for the alternative  $S_N2$  mechanism, the TV-IRC-based reaction profile is valid only in very narrow interval around the TS. The reason is that the TV is mainly the migratory movement of the expelled chloride leaving group that is hydrogen-bonding to one of the C–H bonds.<sup>3</sup> But just before this TS, there is a real  $S_N2$  stage in which the IRC has a large component of the characteristic Pd–C–Cl asymmetric stretch in combination with the methyl umbrella mode, while directly after the TS, the  $S_N2$  reaction path merges into the regular oxidative insertion path.

#### 5. Conclusions

The appearance of a reaction profile associated with the reaction path (defined as the path of steepest descent from

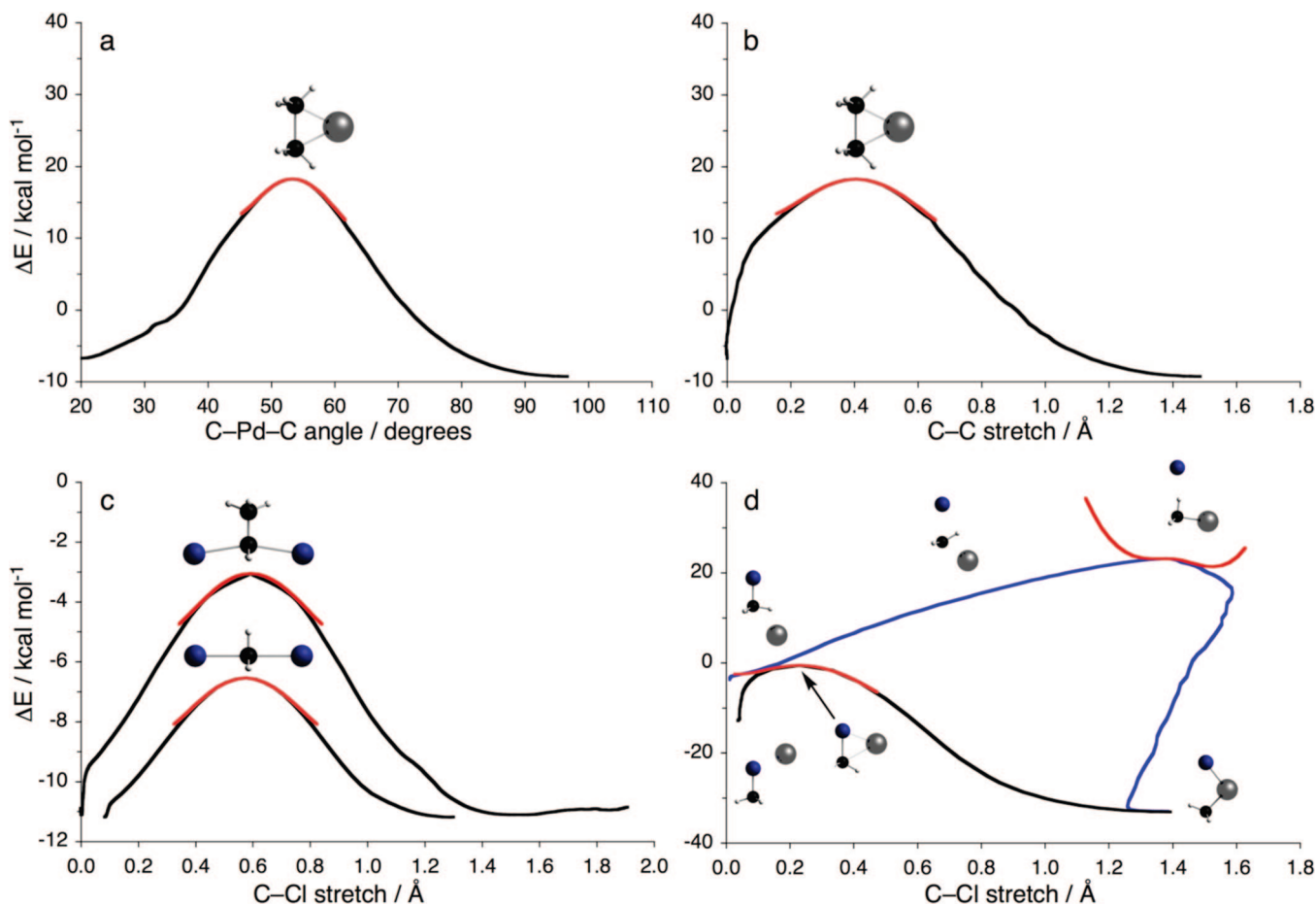


**Figure 5.** Comparison of reaction profiles based on the IRC (black/blue, full curves) and TV-IRC (red, partial curves): (a) oxidative insertion of Pd + ethane with the C-Pd-C angle as a reaction coordinate, (b) oxidative insertion of Pd + ethane with the C-C stretch as a reaction coordinate, (c)  $S_N2$  reactions of  $\text{Cl}^- + \text{CH}_3\text{Cl}$  and  $\text{Cl}^- + \text{CH}_3\text{CH}_2\text{Cl}$  with the C-Cl stretch as a reaction coordinate, and (d) oxidative insertion versus the  $S_N2$  mechanism for oxidative addition of Pd +  $\text{CH}_3\text{Cl}$  (note the breakdown of the TV-IRC approximation in the case of the latter  $S_N2$  mechanism; see text).

the saddle point) depends on the choice of reaction coordinate onto which the IRC is projected. Here, we have shown that the choice of reaction coordinate is critical for zooming in on the important stage of the reaction and for revealing the origin of trends along series of reactions. Some criteria for a good reaction coordinate are (i) a large amplitude in coordinates that define the overall reaction, for example, the C-X bond into which a metal oxidatively inserts, (ii) a large amplitude in the transition vector, that is, the normal mode associated with a negative force constant that leads from the TS to the steepest descent paths, and (iii) preservation of this amplitude over a sufficiently long interval along the reaction path before and after the TS.

Furthermore, we have shown that the transition vector can serve as a useful and computationally much more efficient approximation (designated TV-IRC approximation) for full IRC computations if condition iii is satisfied. We are planning to use this approximation for extended activation-strain analyses<sup>3</sup> of computationally demanding oxidative addition reactions (large substrates and catalyst complexes) through direct insertion of the metal center into the activated bond. We have also shown that the TV-IRC approximation breaks down and can thus not be used for the competing  $S_N2$

pathway of oxidative addition because here condition iii is not satisfied.

**Acknowledgment.** We thank the National Research School Combination-Catalysis (NRSC-C) and The Netherlands Organization for Scientific Research (NWO-CW) for financial support.

**Supporting Information Available:** Graphs of energies as a function of the IRC with the position of the transition state set to zero. This material is available free of charge via the Internet at <http://pubs.acs.org>.

## References

- (1) Ziegler, T.; Autschbach, J. *Chem. Rev.* **2005**, *105*, 2695–2722.
- (2) (a) Bickelhaupt, F. M. *J. Comput. Chem.* **1999**, *20*, 114–128. (b) Diefenbach, A.; de Jong, G. T.; Bickelhaupt, F. M. *Mol. Phys.* **2005**, *103*, 995–998. (c) Bickelhaupt, F. M.; Baerends, E. J.; Nibbering, N. M. M. *Chem.-Eur. J.* **1996**, *2*, 196–207.
- (3) de Jong, G. T.; Bickelhaupt, F. M. *ChemPhysChem* **2007**, *8*, 1170–1181.



- (4) (a) Deng, L. Q.; Ziegler, T. *Int. J. Quantum Chem.* **1994**, 52, 731–765. (b) Deng, L. Q.; Ziegler, T.; Fan, L. Y. *J. Chem. Phys.* **1993**, 99, 3823–3835.
- (5) Fukui, K. *Acc. Chem. Res.* **1981**, 14, 363–368.
- (6) Gonzalez, C.; Schlegel, H. B. *J. Phys. Chem.* **1990**, 94, 5523–5527.
- (7) (a) Ishida, K.; Morokuma, K.; Komornicki, A. *J. Chem. Phys.* **1977**, 66, 2153–2156. (b) Fukui, K. *J. Phys. Chem.* **1970**, 74, 4161–4163.
- (8) Heidrich, D. *The Reaction Path in Chemistry: Current Approaches and Perspectives*; Kluwer Academic Publishers: Dordrecht, The Netherlands, 1995.
- (9) (a) Yang, X. Y.; Wang, Y. C.; Geng, Z. Y.; Liu, Z. Y.; Wang, H. Q. *THEOCHEM* **2007**, 807, 49–54. (b) Sakai, S. *J. Phys. Chem. A* **2006**, 110, 12891–12899. (c) Lu, L. L.; Liu, X. W.; Wang, Y. C.; Wang, H. Q. *THEOCHEM* **2006**, 774, 59–65. (d) Wang, Y. C.; Yang, X. Y.; Geng, Z. Y.; Liu, Z. Y. *Chem. Phys. Lett.* **2006**, 431, 39–44. (e) Wang, Y. C.; Liu, Z. Y.; Geng, Z. Y.; Yang, X. Y. *Chem. Phys. Lett.* **2006**, 427, 271–275. (f) Wang, Y. C.; Liu, Z. Y.; Geng, Z. Y.; Yang, X. Y.; Gao, L. G.; Chen, X. X. *THEOCHEM* **2006**, 765, 27–34. (g) Domingo, L. R.; Picher, M. T.; Arroyo, P. *Eur. J. Org. Chem.* **2006**, 2570–2580. (h) Xie, J.; Feng, D. C.; Feng, S. Y.; Zhang, J. *THEOCHEM* **2005**, 755, 55–63. (i) Shiota, Y.; Yasunaga, M.; Naka, A.; Ishikawa, M.; Yoshizawa, K. *Organometallics* **2004**, 23, 4744–4749. (j) Shiota, Y.; Yoshizawa, K. *J. Chem. Phys.* **2003**, 118, 5872–5879. (k) Sakai, S. *Int. J. Quantum Chem.* **2000**, 80, 1099–1106. (l) Sakai, S. *J. Phys. Chem. A* **2000**, 104, 922–927. (m) Nguyen, L. T.; Le, T. N.; De Proft, F.; Chandra, A. K.; Langenaeker, W.; Nguyen, M. T.; Geerlings, P. *J. Am. Chem. Soc.* **1999**, 121, 5992–6001. (n) Yoshizawa, K.; Shiota, Y.; Yamabe, T. *J. Chem. Phys.* **1999**, 111, 538–545. (o) Su, M. D.; Chu, S. Y. *J. Am. Chem. Soc.* **1999**, 121, 1045–1058. (p) Sakai, S. *Int. J. Quantum Chem.* **1998**, 70, 291–302. (q) Wong, C. K.; Li, W. K.; Baker, J. *THEOCHEM* **1995**, 357, 75–86. (r) Deng, L. Q.; Branchadell, V.; Ziegler, T. *J. Am. Chem. Soc.* **1994**, 116, 10645–10656. (s) Cundari, T. R. *J. Am. Chem. Soc.* **1994**, 116, 340–347. (t) Taketsugu, T.; Hirano, T. *J. Chem. Phys.* **1993**, 99, 9806–9814. (u) Yamabe, S.; Kawajiri, S.; Minato, T.; Machiguchi, T. *J. Org. Chem.* **1993**, 58, 1122–1127.
- (10) (a) Bento, A. P.; Bickelhaupt, F. M. *J. Org. Chem.* **2007**, 72, 2201–2207. (b) van Bochove, M. A.; Swart, M.; Bickelhaupt, F. M. *J. Am. Chem. Soc.* **2006**, 128, 10738–10744.
- (11) van Stralen, J. N. P.; Bickelhaupt, F. M. *Organometallics* **2006**, 25, 4260–4268.
- (12) Baerends, E. J.; Autschbach, J. A.; Bérces, A.; Berger, J. A.; Bickelhaupt, F. M.; Bo, C.; de Boeij, P. L.; Boerrigter, P. M.; Cavallo, L.; Chong, D. P.; Deng, L.; Dickson, R. M.; Ellis, D. E.; Fan, L.; Fischer, T. H.; Fonseca Guerra, C.; van Gisbergen, S. J. A.; Groeneveld, J. A.; Gritsenko, O. V.; Grüning, M.; Harris, F. E.; van den Hoek, P.; Jacobsen, H.; Jensen, L.; Kadantsev, E. S.; van Kessel, G.; Klooster, R.; Kootstra, F.; van Lenthe, E.; McCormack, D. A.; Michalak, A.; Neugebauer, J.; Nicu, V. P.; Osinga, V. P.; Patchkovskii, S.; Philipsen, P. H. T.; Post, D.; Pye, C. C.; Ravenek, W.; Romaniello, P.; Ros, P.; Schipper, P. R. T.; Schreckenbach, G.; Snijders, J. G.; Solà, M.; Swart, M.; Swerhone, D.; te Velde, G.; Vernooijs, P.; Versluis, L.; Visscher, L.; Visser, O.; Wang, F.; Wesolowski, T. A.; van Wezenbeek, E. M.; Wiesenekker, G.; Wolff, S. K.; Woo, T. K.; Yakovlev, A.; Ziegler, T. *ADF2007.01*; SCM: Amsterdam, 2007.
- (13) te Velde, G.; Bickelhaupt, F. M.; Baerends, E. J.; Fonseca Guerra, C.; van Gisbergen, S. J. A.; Snijders, J. G.; Ziegler, T. *J. Comput. Chem.* **2001**, 22, 931–967.
- (14) (a) Becke, A. D. *Phys. Rev. A: At., Mol., Opt. Phys.* **1988**, 38, 3098. (b) Lee, C. T.; Yang, W. T.; Parr, R. G. *Phys. Rev. B: Condens. Matter Mater. Phys.* **1988**, 37, 785–789.
- (15) Baerends, E. J.; Ellis, D. E.; Ros, P. *Chem. Phys.* **1973**, 2, 41.
- (16) van Lenthe, E.; Baerends, E. J.; Snijders, J. G. *J. Chem. Phys.* **1994**, 101, 9783–9792.
- (17) (a) de Jong, G. T.; Bickelhaupt, F. M. *J. Chem. Theory Comput.* **2006**, 2, 322–335. (b) de Jong, G. T.; Geerke, D. P.; Diefenbach, A.; Solà, M.; Bickelhaupt, F. M. *J. Comput. Chem.* **2005**, 26, 1006–1020.
- (18) van Zeist, W. J.; Fonseca Guerra, C.; Bickelhaupt, F. M. *J. Comput. Chem.* **2008**, 29, 312–315.
- (19) (a) Fonseca Guerra, C.; Handgraaf, J. W.; Baerends, E. J.; Bickelhaupt, F. M. *J. Comput. Chem.* **2004**, 25, 189–210. (b) Bickelhaupt, F. M.; van Eikema Hommes, N. J. R.; Fonseca Guerra, C.; Baerends, E. J. *Organometallics* **1996**, 15, 2923–2931.
- (20) Taichibana, A.; Fukui, K. *Theor. Chim. Acta* **1979**, 51, 189–206.

CT700214V